Atomic view of cosolute-induced protein denaturation probed by NMR solvent paramagnetic relaxation enhancement

Yusuke Okuno[a], Janghyun Yoo[a], Charles D. Schwieters[a], Robert B. Best[a] (ID), Hoi Sung Chung[a] (ID), and G. Marius Clore[a,1] (ID)

[a]Laboratory of Chemical Physics, National Institute of Diabetes and Digestive and Kidney Diseases, National Institutes of Health, Bethesda, MD 20892-0520

The cosolvent effect arises from the interaction of cosolute molecules with a protein and alters the equilibrium between native and unfolded states. Denaturants shift the equilibrium toward the latter, while osmolytes stabilize the former. The molecular mechanism whereby cosolutes perturb protein stability is still the subject of considerable debate. Probing the molecular details of the cosolvent effect is experimentally challenging as the interactions are very weak and transient, rendering them invisible to most conventional biophysical techniques. Here, we probe cosolute–protein interactions by means of NMR solvent paramagnetic relaxation enhancement together with a formalism we recently developed to quantitatively describe, at atomic resolution, the energetics and dynamics of cosolute–protein interactions in terms of a concentration normalized equilibrium average of the interspin distance, $\langle r^{-6}\rangle_{norm}$, and an effective correlation time, τ_c. The system studied is the metastable drkN SH3 domain, which exists in dynamic equilibrium between native and unfolded states, thereby permitting us to probe the interactions of cosolutes with both states simultaneously under the same conditions. Two paramagnetic cosolute denaturants were investigated, one neutral and the other negatively charged, differing in the presence of a carboxyamide group versus a carboxylate. Our results demonstrate that attractive cosolute–protein backbone interactions occur largely in the unfolded state and some loop regions in the native state, electrostatic interactions reduce the $\langle r^{-6}\rangle_{norm}$ values, and temperature predominantly impacts interactions with the unfolded state. Thus, destabilization of the native state in this instance arises predominantly as a consequence of interactions of the cosolutes with the unfolded state.

protein–cosolute interactions | transient states | drkN SH3 native and unfolded states | NMR relaxation | replica exchange molecular dynamics

Cosolutes (also known as cosolvents) modulate the stability and function of proteins acting either as denaturants or osmolytes that shift the conformational equilibrium of a protein toward either the unfolded or native states, respectively (1). The mechanism of the cosolvent effect whereby cosolutes perturb the folding/unfolding equilibrium has been discussed for more than half a century (1–8), yet the exact mechanism of the cosolvent effect has not been satisfactorily explained even for urea, the most commonly studied cosolute. The difficulty in characterizing the cosolvent effect lies in the extremely weak interaction strengths between cosolutes and protein with equilibrium dissociation constants in excess of 1 M (9). Indeed, in some instances a negative binding stoichiometry has been observed, implying that a simple binding model does not provide an appropriate description of the cosolvent effect (9, 10). Alternative binding models have been proposed (3, 10), but no model involving stoichiometric binding has succeeded in explaining the cosolvent effect (11). This may in part be due to the possibility that cosolutes can adopt different coordinations at the protein surface under various conditions (such as concentration and pH) (7, 12).

Direct experimental detection of weak, highly transient, sparsely populated interactions between cosolute and protein at

atomic resolution is difficult using standard spectroscopic techniques such as infrared or conventional NMR spectroscopy. Furthermore, the lack of adequate theoretical models to interpret the experimental data has hampered progress toward understanding the mechanism of the cosolvent effect. Experimental information regarding the molecular details of the cosolvent effect has largely been limited to studies of the interaction of cosolutes with "peptide fragments," such as free amino acids and tripeptides (13–17) interpreted in terms of Tanford's group transfer free energy model (2, 3). The impact of complexity arising from three-dimensional protein structure, chain connectivity, and highly diverse protein surfaces, on the other hand, has mainly been explored by computer simulations (18–23), although the coupling of change in denatured state collapse to interactions with denaturants has been modeled via a combination of Förster resonance energy transfer (FRET) spectroscopy and polymer theory (6, 24). It has not, however, been possible to study the interaction of denaturants with proteins at high resolution.

Here, we make use of NMR solvent paramagnetic relaxation enhancement (sPRE) (25–29) to directly study the interaction between paramagnetic cosolutes and protein backbone amide protons at atomic resolution. The system we chose to examine is the metastable drkN SH3 protein domain (30–34), which exists in a dynamic equilibrium between native and unfolded states that is slow on the chemical shift timescale, thereby permitting one to obtain sPRE data for both states simultaneously under identical

Significance

The cosolvent effect alters the equilibrium between native and unfolded states of a protein, with denaturant cosolutes shifting the equilibrium toward the latter and osmolyte cosolutes stabilizing the former. Quantitative characterization of the strength of cosolute–protein interactions at atomic resolution is experimentally challenging as these interactions are highly transient and occur at low occupancy. Here, we make use of paramagnetic cosolutes and NMR solvent paramagnetic relaxation enhancement measurements to quantify the interaction of cosolutes with drkN SH3, a metastable protein domain that exists in dynamic equilibrium between native and unfolded states. The current study shows that destabilization of the native state is largely attributable to preferential cosolute interactions with the unfolded state.

experimental conditions (Fig. 1). The paramagnetic cosolutes chosen were 3-carbamoyl and 3-carboxy PROXYL, which differ in the presence of a neutral carboxyamide group and a negatively charged carboxylate group, respectively (Fig. 2*A*). The theoretical framework used to quantitatively analyze the sPRE data is one we recently described (28) that is not dependent on the stoichiometric binding model and yields two residue-specific parameters that describe the energetics and dynamics of cosolute–protein interactions at atomic resolution: Specifically, a concentration normalized equilibrium average of the interspin distance, $\langle r^{-6} \rangle_{norm}$, and an effective correlation time τ_c (Fig. 1). The former depends not only on the excluded volume interactions between protein and cosolute but also on site-specific intermolecular forces (e.g., hydrophobic and electrostatic interactions). We quantitatively show how the two paramagnetic cosolutes are distributed on the surface of the native and unfolded states of drkN SH3, probe the impact of electrostatics on protein–cosolute interactions by comparing the results obtained with the neutral and negatively charged paramagnetic cosolutes, and explore the effect of temperature to provide further insight into the physical nature of the interactions.
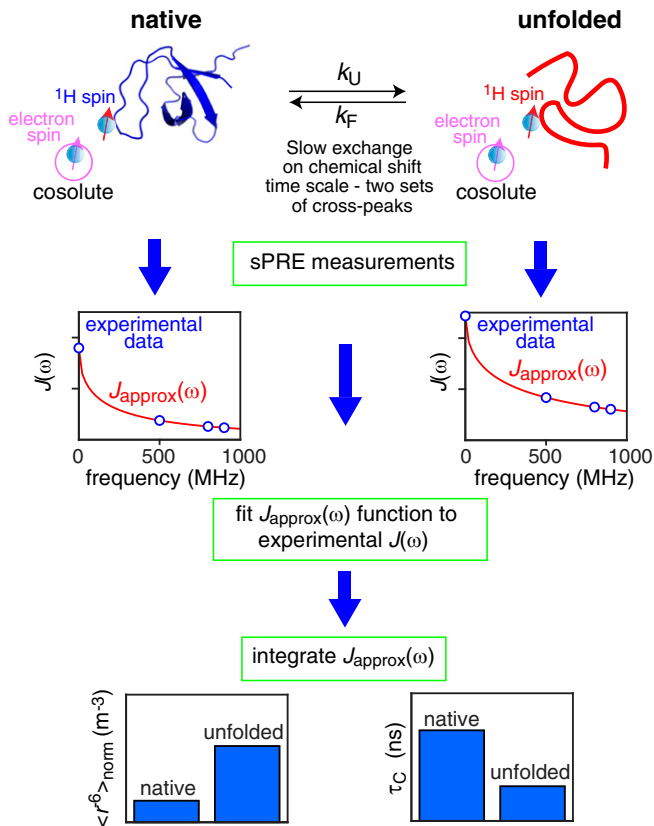

Fig. 1. Summary of overall strategy employed to study cosolute interactions with native and unfolded drkN SH3 at atomic resolution. The native and unfolded states are in slow exchange on the chemical shift timescale enabling solvent PREs (sPREs) arising from paramagnetic cosolutes (3-carbamoyl and 3-carboxy PROXYL) to be measured simultaneously on individual backbone amide protons for both states. The experimental spectral density function, $J(\omega)$, is mapped at several frequencies by measuring the transverse (zero frequency) and longitudinal (at several spectrometer frequencies) sPREs on each amide proton. The experimental data are then fitted to an ansatz spectral density function, $J_{approx}(\omega)$, integration of which yields two residue-specific parameters that describe the energetics (measured as a concentration normalized equilibrium average of the interspin distance between the electron spin on the cosolute and the ^{1}H spin on the protein, $\langle r^{-6} \rangle_{norm}$) and dynamics (provided by an effective correlation time τ_c) of cosolute–protein interactions at atomic resolution.
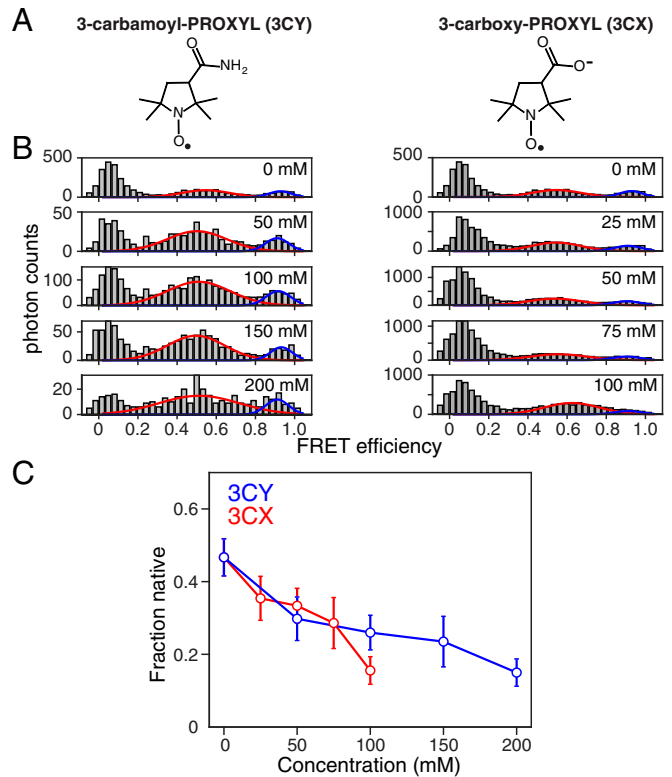

Fig. 2. Probing the effect of neutral and negatively charged paramagnetic cosolutes on the folding/unfolding equilibrium of drkN SH3 by smFRET. (*A*) Structures of the two paramagnetic cosolutes employed in the current work: 3-carbamoyl-PROXYL (3CY, neutral) and 3-carboxy-PROXYL (3CX, negatively charged). The location of the unpaired electron is indicated by the black dot. (*B*) smFRET efficiency histogram as a function of paramagnetic cosolute concentration: *Left*, 3-carbamoyl PROXYL; *Right*, 3-carboxy PROXYL. (*C*) Fraction native population as a function of paramagnetic cosolute concentration (blue, 3-carbamoyl PROXYL; red, 3-carboxy PROXYL) derived from analysis of the smFRET data. Details of the experimental conditions and analysis are provided in *SI Appendix*.

Theory

We first present a brief overview of the theoretical framework developed by Okuno et al. (28) to quantitatively extract energetic and dynamic information on cosolute–protein interactions from sPRE measurements. Relaxation due to direct dipole–dipole interaction between a proton spin on the protein and the electron spin on the paramagnetic cosolute in an isotropic liquid is described by the time correlation function $C(t)$ given by

$$C(t) = N_S \left\langle \frac{P_2(\hat{r}(0) \cdot \hat{r}(t))}{r^3(0)r^3(t)} \right\rangle, \quad [1]$$

where r and $\hat{r}$ denote the length and orientation of a vector, $\vec{r}$, between the unpaired electron on the paramagnetic cosolute and a proton spin on the protein in an arbitrary coordinate frame; $P_2(x)$ is the second-order Legendre polynomial; N_S is the number of cosolute molecules; and the angular brackets $\langle \rangle$ denote an equilibrium average of all positions and orientations of the protein–cosolute pair. The spectral density $J(\omega)$ is defined as the cosine transform of Eq. **1**:

$$J(\omega) = \int_0^\infty C(t)\cos(\omega t)dt. \quad [2]$$

The proton longitudinal (Γ_1) and transverse (Γ_2) sPRE rates, obtained by taking the difference in the proton longitudinal (R_1)

and transverse (R_2) relaxation rates, respectively, in the presence and absence of paramagnetic cosolute, are related to the spectral density $J(\omega)$ by

$$\Gamma_1(\omega_H) = \frac{3}{10}\left(\frac{\mu_o}{4\pi}\right)^2 \hbar^2 \gamma_H^2 \gamma_e^2 J(\omega_H), \qquad [3]$$

and

$$\Gamma_2(\omega_H) = \frac{1}{5}\left(\frac{\mu_o}{4\pi}\right)^2 \hbar^2 \gamma_H^2 \gamma_e^2 \left(J(0) + \frac{3}{4}J(\omega_H)\right), \qquad [4]$$

where μ_o is the vacuum permittivity constant; $\hbar$, Planck's constant divided by 2π; γ_H, the proton gyromagnetic ratio; γ_e, the electron gyromagnetic ratio; and ω_H, the Larmor proton frequency at a given spectrometer field. $J(\omega_H)$ is directly proportional to $\Gamma_1(\omega_H)$; and, from Eqs. 3 and 4, the field independent value of $J(0)$ can be calculated directly from the experimental Γ_1 and Γ_2 values:

$$J(0) = \frac{5\left(\Gamma_2(\omega_H) - \Gamma_1(\omega_H)/2\right)}{(\mu_0/4\pi)^2 \hbar^2 \gamma_H^2 \gamma_e^2}. \qquad [5]$$

Next, we define the concentration-independent equilibrium average $\langle r^{-6}\rangle_{\mathrm{norm}}$, which provides a direct measure of the strength of the interaction between the cosolute and a given proton on the protein:

$$\langle r^{-6}\rangle_{\mathrm{norm}} = \frac{C(0)}{n_S} = 4\pi \int_0^\infty \frac{\exp(-\beta U(r))}{r^4}\, dr, \qquad [6]$$

where $U(r)$ is the potential of the mean force; $\beta = 1/k_B T$, where k_B and T are the Boltzman constant and temperature, respectively; and n_S is the number density (i.e., N_S per unit volume or concentration) of the paramagnetic cosolute. (Note that $\langle r^{-6}\rangle_{\mathrm{norm}}$ has units of meters^{-3}). $\langle r^{-6}\rangle_{\mathrm{norm}}$ is determined not only by the excluded volume interactions between protein and cosolute but also by additional site-specific intermolecular forces arising from electrostatic and hydrophobic interactions. The contribution from excluded volume interactions, $\langle r^{-6}\rangle_{\mathrm{norm}}^{\mathrm{exc}}$, can be calculated directly from molecular coordinates: in the case of the native state from X-ray or NMR coordinates; for the unfolded state from an ensemble of conformations obtained by molecular dynamics (MD) simulations (see *SI Appendix* for details). When $\langle r^{-6}\rangle_{\mathrm{norm}}$ is larger than $\langle r^{-6}\rangle_{\mathrm{norm}}^{\mathrm{exc}}$, local attractive interactions are present; if $\langle r^{-6}\rangle_{\mathrm{norm}}$ is smaller than $\langle r^{-6}\rangle_{\mathrm{norm}}^{\mathrm{exc}}$, then local repulsive interactions are present. Thus, $\langle r^{-6}\rangle_{\mathrm{norm}}$ can be used to identify the types of interactions (attractive, no force or repulsive) between cosolute and individual protons in the protein.

If $J(\omega)$ were known at a continuum of frequencies, $\langle r^{-6}\rangle_{\mathrm{norm}}$ could be determined from the inverse cosine transform of Eq. 2 at $t = 0$,

$$\langle r^{-6}\rangle_{\mathrm{norm}} = \frac{2}{n_S \pi}\int_0^\infty J(\omega)\,d\omega. \qquad [7]$$

In practice, however, only a small number of spectrometer frequencies and hence $J(\omega_H)$ values are available.

For the sPRE the spectral density is not Lorentzian owing to translational diffusion (35–38). To account for this behavior, the approach we therefore developed to quantitatively analyze Γ_1 and Γ_2 data is based on global fitting of the sPRE data for all measurable residues at only a few NMR spectrometer fields using the following ansatz for the spectral density, $J_{\mathrm{approx}}(\omega)$, which reproduces the first two and first terms in the low- and high-frequency expansion of $J(\omega)$, respectively (28):

$$J_{\mathrm{approx}}(\omega) = \frac{J(0)}{\left(1 + a\omega + b\sqrt{\omega}\right)^2}, \qquad [8]$$

where a is a site-specific fitted parameter, b is given by

$$b = \frac{\sqrt{2}\pi n_S}{9 D_{\mathrm{trans}}^{3/2} J(0)}, \qquad [9]$$

and the relative translational diffusion coefficient, D_{trans}, for the interacting molecules is either treated as a globally fitted parameter (when sPRE data have been measured at multiple spectrometer fields) or can be independently determined experimentally from NMR pulse field gradient diffusion experiments (if sPRE data at only a single field are available). Once the site-specific values of a and b are determined, the site-specific values of $\langle r^{-6}\rangle_{\mathrm{norm}}$ can be obtained by analytical evaluation of the integral in Eq. 7 (28).

An effective site-specific correlation time, τ_C, which provides a measure of the timescale of the fluctuations of the interspin vector $\vec{r}$ that arises from both translational and rotational diffusion and is influenced by both short- and long-range intermolecular interactions, can then be calculated from the $\langle r^{-6}\rangle_{\mathrm{norm}}$ values as

$$\tau_C = \frac{\int_0^\infty C(t)\,dt}{C(0)} = \frac{J(0)}{n_S \langle r^{-6}\rangle_{\mathrm{norm}}}. \qquad [10]$$

Results and Discussion

3-Carbamoyl and 3-Carboxy PROXYL Denature drkN SH3. We first investigated the effect of 3-carbamoyl and 3-carboxy-PROXYL on the thermodynamic stability of drkN SH3. Since both paramagnetic cosolutes exhibit substantial absorption in the UV region at high concentration, simple bulk spectroscopic techniques such as circular dichroism or tryptophan fluorescence could not be used. Likewise, it was not possible to simply follow the intensity of native and unfolded cross-peaks in ^{1}H–^{15}N NMR correlation spectra as the cosolutes give rise to substantial line broadening as a result of the sPRE effect. To circumvent these issues, we therefore resorted to single-molecule FRET (smFRET) by labeling the N- and C-termini of drkN SH3 with the green and far-red fluorescent probes Alexa Fluor 488 and Alexa Fluor 647, respectively.

smFRET efficiency diagrams for fluorophore-labeled drkN SH3 as a function of paramagnetic cosolute concentration are shown in Fig. 2B. Note that fluorescence of the Alexa dyes was also quenched by the paramagnetic cosolute necessitating the use of appropriate corrections to extract the populations of native and unfolded states (see *SI Appendix* for details and *SI Appendix*, Fig. S1). The population of native state of fluorophore-labeled drkN SH3 in the absence of paramagnetic cosolute is 47% (at 22 °C) (Fig. 2C), which is qualitatively consistent with a population of ~29% for wild-type drkN SH3 under similar buffer conditions at 25 °C obtained by NMR (see following section). Upon addition of increasing amounts of either 3-carbamoyl or 3-carboxy PROXYL cosolutes, the fraction of native drkN SH3 is progressively reduced and the folding/unfolding equilibrium is shifted toward the unfolded state (Fig. 2C). Thus, both paramagnetic cosolutes can be classified as denaturants. Interestingly, the degree of denaturation is similar for the two paramagnetic cosolutes despite their difference in charge.

sPRE Measurements on Native and Unfolded drkN SH3. The ^{1}H$_N$-Γ_2 and Γ_1 sPRE profiles observed on ^{2}H/^{15}N-labeled drkN SH3 at two temperatures (298 and 277 K) in the presence of 25 mM 3-carbamoyl and 3-carboxy PROXYL are shown in Fig. 3 A and B, respectively. A concentration of 25 mM was chosen for the

Okuno et al.
Atomic view of cosolute-induced protein denaturation probed by NMR solvent paramagnetic relaxation enhancement

PNAS | 3 of 9
https://doi.org/10.1073/pnas.2112021118
www.manaraa.com

BIOPHYSICS AND COMPUTATIONAL BIOLOGY

CHEMISTRY

paramagnetic cosolutes since this is sufficient to generate sPREs that can be measured at high accuracy, while minimally perturbing the folding/unfolding equilibrium (Fig. 2). Furthermore, at this concentration of cosolute, $^1H_N/^{15}N$ chemical shift perturbations, as expected for very weak intermolecular interactions (39), are negligibly small for both the native and unfolded states (*SI Appendix*, Fig. S2), reflecting the absence of any significant backbone structural changes as well as low occupancy of transiently bound cosolutes.

The ^1H_N-Γ_2 data, which are dominated by $J(0)$ (see Eq. **4**), were recorded at 500 MHz; the ^1H_N-Γ_1 data, which are proportional to $J(\omega_H)$ (see Eq. **3**), were recorded at three fields (500, 800, and 900 MHz) for 3-carbamoyl PROXYL and two fields (500 and 900 MHz) for 3-carboxyl-PROXYL. It should be noted that it is important when analyzing the experimental ^1H_N-R_1 and R_2 decay curves, to take exchange between native and unfolded states into account under conditions where the overall exchange rate, k_{ex} is comparable to or larger than ^1H_N-R_1 and R_2, respectively (see *SI Appendix*, Eqs. S11 and S12). k_{ex} (= k_F + k_U, where k_F and k_U are the folding and unfolding rate constants, respectively) can be readily determined by $^{15}N_z$ exchange experiments (40). At 298 K, $k_{ex} \sim 4$ s^{-1} (k_F = 1.13 $\pm$ 0.05 s^{-1}; k_U = 2.83 $\pm$ 0.06 s^{-1}; population of native state ~29%; see *SI Appendix*, Fig. S3*A*) and exchange therefore has to be taken into account to extract accurate ^1H_N-Γ_1 and Γ_2 values; at 277 K, however, exchange is an order of magnitude slower ($k_{ex} \sim 0.34$ s^{-1}; k_F = 0.09 $\pm$ 0.01 s^{-1}; $k_U \sim 0.25 \pm 0.01$ s^{-1}; population of native state ~26%; *SI Appendix*, Fig. S3*B*), and its impact is therefore insignificant (*SI Appendix*, Fig. S4).

$\langle r^{-6} \rangle_{norm}$ and τ_C Profiles. As described in *Theory*, the sPRE data allow one to derive two physical measures of the energetics and dynamics of cosolute–protein interactions at the residue-specific atomic level: namely, the concentration normalized equilibrium average of the interspin distance, $\langle r^{-6} \rangle_{norm}$ (Eq. **7**) and an effective correlation time τ_c (Eq. **10**), respectively, through the use of the approximate spectral density function given by Eq. **8**. The experimental ^1H_N-Γ_1 and Γ_2 data (expressed in terms of Eqs. **3** and **4**, respectively) are globally fit to Eq. **8** optimizing site-specific parameters a, and a global parameter for the relative translational diffusion coefficient of the two interacting molecules (D_{trans}; Eq. **9**). The values for the latter are fully consistent with experimental D_{trans} values determined independently by pulse field gradient diffusion NMR (see *SI Appendix*, Figs. S5 and S6 and Table S1).

The $\langle r^{-6} \rangle_{norm}$ and τ_C profiles are shown in Fig. 4. To permit easy comparison with the $\langle r^{-6} \rangle_{norm}^{exc}$ values calculated directly from atomic coordinates on the assumption of only excluded volume interactions (see *SI Appendix* for details), the $\langle r^{-6} \rangle_{norm}$ profiles are plotted on a logarithmic scale. The corresponding $[\langle r^{-6} \rangle_{norm} - \langle r^{-6} \rangle_{norm}^{exc}]$ profiles are shown in Fig. 5 *A* and *B*. The latter subtract the contribution from excluded volume interactions and thus provide a direct quantitative measure of the preferential interactions between cosolute and protein atoms (i.e., positive value, attractive interaction; negative value, repulsive interaction).

Considering the native state of drkN SH3, almost all of the backbone amide protons display positive values of $[\langle r^{-6} \rangle_{norm} - \langle r^{-6} \rangle_{norm}^{exc}]$ indicative of attractive interactions (Figs. 4 and 5 *A* and *B*). Ser10, Asn14, and Asn51 for both paramagnetic cosolutes and Ser34 for 3-carboxyamide PROXYL have particularly high values of $\langle r^{-6} \rangle_{norm}$ and large positive values of $[\langle r^{-6} \rangle_{norm} - \langle r^{-6} \rangle_{norm}^{exc}]$ (Fig. 5). All these residues are located in loops. In contrast, residues within the β-sheets have ^1H_N-Γ_1 values close to zero (Fig. 3), and although quantitative analysis was not possible for all β-strand residues, they are expected to have low $\langle r^{-6} \rangle_{norm}$ values as both
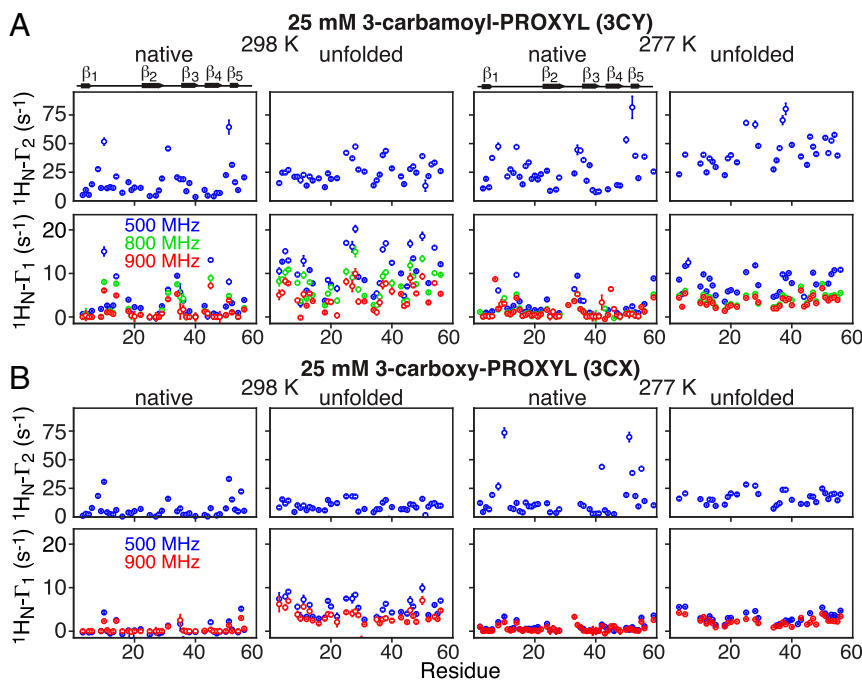

Fig. 3. Experimental backbone amide sPRE profiles for native and unfolded drkN SH3 in the presence of neutral and negatively charged paramagnetic cosolutes. sPRE data were obtained for 0.2 mM $^2H/^{15}N$-labeled drkN SH3 in the presence of 25 mM (*A*) 3-carbamoyl PROXYL and (*B*) 3-carboxy PROXYL paramagnetic cosolutes at 298 (*Left*) and 277 (*Right*) K. *Top* and *Bottom* display the experimental ^1H_N-Γ_2 and ^1H_N-Γ_1 profiles, respectively, measured at 500 (blue), 800 (green), and 900 (red) MHz. The ^1H_N-R_1 and R_2 rates at 298 K, used to calculate the sPRE values, are corrected to take into account chemical exchange between the native and unfolded states (*SI Appendix* and *SI Appendix*, Fig. S3); at 277 K exchange between native and unfolded states is too slow to impact the measured ^1H_N relaxation data and calculated $\langle r^{-6} \rangle_{norm}$ values (*SI Appendix*, Fig. S4). The location of the β-strands in the native state is shown at the *Top* of *A*: strands β1, β2, β3, β4, and β5 comprise residues 2–5, 23–29, 36–41, 44–49, and 53–55, respectively.
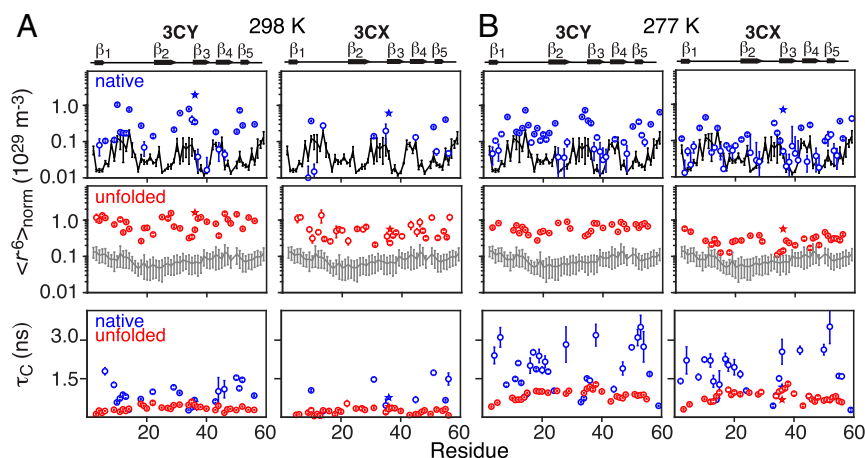
Fig. 4. Experimentally derived $\langle r^{-6}\rangle_{norm}$ and τ_C profiles obtained from the analysis of sPRE measurements on native and unfolded drkN SH3 in the presence of neutral and negatively charged paramagnetic cosolutes. Data were acquired at two temperatures: (*A*) 298 and (*B*) 277 K. The experimentally derived values are shown as circles, with the exception of those for the side-chain $N_{\varepsilon 1}H$ indole proton of Trp36, which are represented by a star. $\langle r^{-6}\rangle_{norm}$ values with errors > 7×10^{28} m^{-3} and τ_C values with errors > 0.75 ns have been excluded from the plots. The sPRE data used to calculated $\langle r^{-6}\rangle_{norm}$ and τ_c were collected on 0.2 mM ^{2}H/^{15}N-labeled drkN SH3 in the presence of 25 mM 3-carbamoyl (3CY, neutral) or 3-carboxy (3CX, negative) PROXYL. For comparison, the $\langle r^{-6}\rangle_{norm}^{exc}$ profiles calculated directly from the coordinates of drkN SH3 in the native [PDB ID code 2AZS (32)] and unfolded states (see *SI Appendix* for details), taking into account only the excluded volume with no intermolecular forces between protein and cosolute, are displayed as continuous black and gray lines, respectively. The $\langle r^{-6}\rangle_{norm}^{exc}$ values in the native state were calculated for the 10 NMR structures deposited in the 2AZS coordinates to account for different surface side-chain conformers, and the error bars (black vertical lines) represent the SDs among these 10 structures. Similarly, for the unfolded state $\langle r^{-6}\rangle_{norm}^{exc}$ profiles, the error bars represent the SDs among the 505 structure snapshots obtained from the replica exchange MD trajectory at either 298 or 277 K (see *SI Appendix* for details; also note there is no noticeable difference in the $\langle r^{-6}\rangle_{norm}^{exc}$ values of the unfolded state ensemble calculated from the MD simulations at 298 and 277 K; see *SI Appendix*, Fig. S7*B*).

^{1}H$_N$-Γ_2 and ^{1}H$_N$-Γ_1 are small. These results would not be inconsistent with transient hydrogen bonding to exposed regions of the protein backbone driving favorable association of cosolutes. We also note that some residues, such as Met30, Asp42, and Met55, not included in the analysis, due to either low cross-peak intensities or cross-peak overlap, are expected to have a high $\langle r^{-6}\rangle_{norm}$ values but are not shown in Figs. 4 and 5.

Comparison of the $\langle r^{-6}\rangle_{norm}$ and $[\langle r^{-6}\rangle_{norm} - \langle r^{-6}\rangle_{norm}^{exc}]$ profiles for the native and unfolded states of drkN SH3 observed with 3-carbamoyl PROXYL at both 298 and 277 K clearly show that, overall, 3-carbamoyl PROXYL interacts preferentially with the unfolded state relative to the native state (Figs. 4*A* and 5*A*). The same is true of 3-carboxy PROXYL, although the differential

between native and unfolded states is less marked (Figs. 4 and 5*B*). The preferential interaction of both cosolutes with the unfolded state makes intuitive sense as solvent exposure for the majority of backbone amide protons in the unfolded state is higher than that for the native state resulting in correspondingly higher $\langle r^{-6}\rangle_{norm}^{exc}$ values (compare the gray lines depicting the $\langle r^{-6}\rangle_{norm}^{exc}$ profile for the unfolded state shown in the *Middle* panels of Fig. 4 with the black ones for the native state shown in the *Top* panels of Fig. 4). That being said, the $\langle r^{-6}\rangle_{norm}$ values for the most exposed loop regions in the native state (e.g., residues 10–14) are comparable to those for the unfolded state (Fig. 4). The $\langle r^{-6}\rangle_{norm}^{exc}$ for the unfolded state of course depends on the ensemble of structures
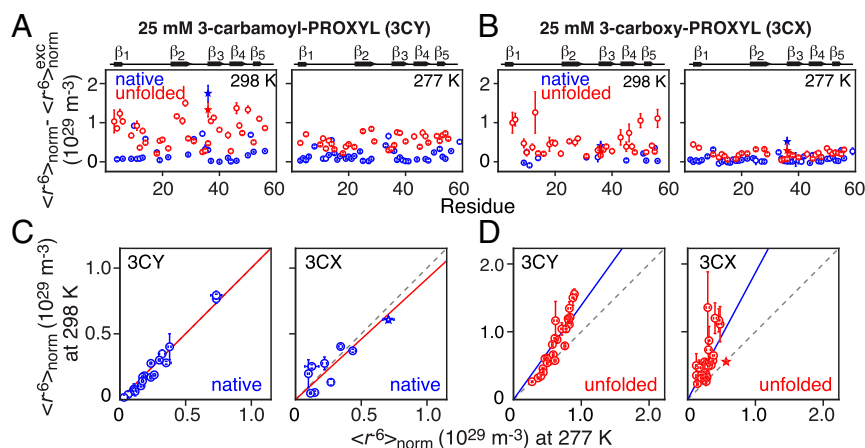

Fig. 5. Mapping sites of preferential interaction of neutral and negatively charge paramagnetic cosolutes with the native and unfolded states of drkN SH3. (*A*) $\left[\langle r^{-6}\rangle_{norm} - \langle r^{-6}\rangle_{norm}^{exc}\right]$ profiles obtained for (*A*) 3-carbamoyl PROXYL (3CY, neutral) and (*B*) 3-carboxy PROXYL (3CX, negative) at 298 and 277 K. Correlation between $\langle r^{-6}\rangle_{norm}$ values obtained at 298 and 277 K for the (*C*) native and (*D*) unfolded states of drkN SH3. The experimentally derived values are shown as circles, with the exception of those for the side-chain $N_{\varepsilon 1}H$ indole proton of Trp36, which are represented by a star. The continuous lines in panels (*C* and *D*) are the best-fits to the linear relationship $y = mx$.

chosen for the calculation—in this case, we have used replica exchange molecular simulations with a force field that has been shown to accurately reproduce unfolded state properties (41); additional confidence is given by the excellent agreement between calculated and experimental FRET efficiencies of the unfolded state in absence of cosolutes, 0.55 and 0.53 (Fig. 2*B*), respectively.

In addition to backbone amide protons, we also analyzed the sPRE data for the side-chain $N_{\varepsilon 1}H$ indole proton of Trp36 (indicated by the star symbol in Figs. 4 and 5 *A* and *B*). Trp36 is solvent exposed in both native and unfolded states (42–44). The $\langle r^{-6} \rangle_{norm}$ and $[\langle r^{-6} \rangle_{norm} - \langle r^{-6} \rangle_{norm}^{exc}]$ values for the indole $N_{\varepsilon 1}H$ proton of Trp36 are comparable to the largest values observed for the backbone amide protons, indicating that the side chain of Trp36 experiences similar preferential interactions with cosolutes, consistent with the hypothesis that solvent-exposed side chains play a significant role in the cosolvent effect (23, 45).

Contribution of Electrostatics to Cosolute–Protein Interactions. The contribution of electrostatics to interactions of the cosolutes with the native and unfolded states of drkN SH3 can be assessed experimentally from a comparison of the data obtained with 3-carbamoyl (charge = 0) and 3-carboxy (charge = −1) PROXYL (Fig. 6). The $\langle r^{-6} \rangle_{norm}$ values obtained with 3-carboxy PROXYL are overall smaller than those obtained with 3-carbomoyl PROXYL in both the native (Fig. 6*A*) and unfolded (Fig. 6*B*) states. This result is expected as the drkN SH3 has a net charge of about −6, and hence, some contribution from repulsive Coulombic interactions would be expected for 3-carboxy PROXYL.

To obtain further insight into the contribution from electrostatics to cosolute–protein interactions in the native and unfolded states of drkN SH3, we used MD simulations with 18 mM NaCl, corresponding to the experimental ionic strength in the absence of cosolutes (46) (see *SI Appendix* for details) and calculated the local preferential interaction coefficient for the Cl^- ion given by (47)

$$\Lambda_{IP} = \left\langle n_I^P - n_W^P \left(\frac{n_I^B}{n_W^B} \right) \right\rangle, \quad [11]$$

where n_I^P and n_W^P are the number of ions and water molecules, respectively, within 8 Å of a protein backbone amide nitrogen atom, and n_I^B and n_W^B, the number of ions and water molecules further than 8 Å from a backbone nitrogen atom. Λ_{IP} measures

the difference between the observed number of cosolute molecules in the vicinity of the protein, n_I^P, and the number expected if the concentration of cosolute near the protein was the same as in the bulk (second term in Eq. **11**). Partitioning Λ_{IP} into group contributions yields a measure of the relative ion accumulation around the vicinity of each backbone amide group versus bulk solvent. The calculated Λ_{IP} profiles for native and unfolded drkN SH3 are shown in Fig. 7*A* (*Top*). For native and unfolded states, there is background weak exclusion of Cl^- ions. However, Cl^- ions are strongly excluded in the native state from the backbone amide groups of Asp14, Asp33, Gly43, and Lys44 at 298 K and of Gly43, Gly46, and Leu47 at 277 K. In contrast, for the unfolded state, there are regions where Cl^- ions are strongly accumulated and others where they are excluded at both 298 and 277 K. Moreover, when one focuses exclusively on the space around the backbone amide nitrogen atoms, it can be seen that Cl^- ions are not necessarily excluded from negatively charged residues or accumulated around positively charged ones.

The sPRE experimental corollary of Λ_{IP} is provided by $\Delta \langle r^{-6} \rangle_{norm}$, given by the difference in $\langle r^{-6} \rangle_{norm}$ values obtained with 3-carboxylate and 3-carbamoyl PROXYL (Fig. 7*A*, *Bottom*, and Fig. 7*B*). Overall, the $\Delta \langle r^{-6} \rangle_{norm}$ profiles are slightly negative for both native and unfolded states, indicating that, for many residues, 3-carboxylate PROXYL interacts more weakly with the protein backbone than 3-carbamoyl PROXYL, which is qualitatively consistent with the corresponding Λ_{IP} profiles. Thus, it is reasonable to conclude that electrostatic interactions contribute, at least in part, to the origin of the overall smaller values of $\langle r^{-6} \rangle_{norm}$ for 3-carboxylate PROXYL versus 3-carbamoyl PROXYL. It should be noted, however, that both paramagnetic cosolutes comprise a hydrophobic nitroxide group as well as polar groups (carbamoyl or carboxylic acid), and solvation effects on the protein interaction may be different for chloride and 3-carboxylate PROXYL. Thus, any comparison of Λ_{IP} with $\Delta \langle r^{-6} \rangle_{norm}$ should only be considered qualitatively.

It is also important to bear in mind that the effect of charge on the cosolvent effect is complex. For example, although the folding/unfolding equilibrium for drkN SH3 is impacted by the addition of cosolutes of different charge, arginine and lysine, both of which bear a single positive charge, have substantially different effects on protein stability, while acetate (charge −1) and glycine (neutral) exhibit similar effects on protein stability as lysine (48). From the smFRET data reported here (Fig. 2),
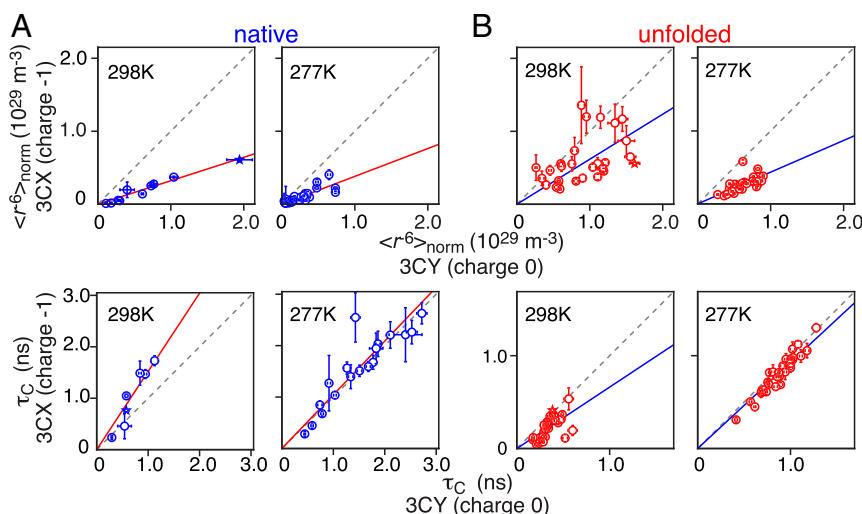

Fig. 6. Correlation of $\langle r^{-6} \rangle_{norm}$ and τ_C values obtained with 3-carbamoyl and 3-carboxy PROXYL paramagnetic cosolutes. Correlations for the (*A*) native and (*B*) unfolded states of drkN SH3 at two temperatures (298 and 277 K). The continuous lines are the best-fits to the linear relationship $y = mx$.
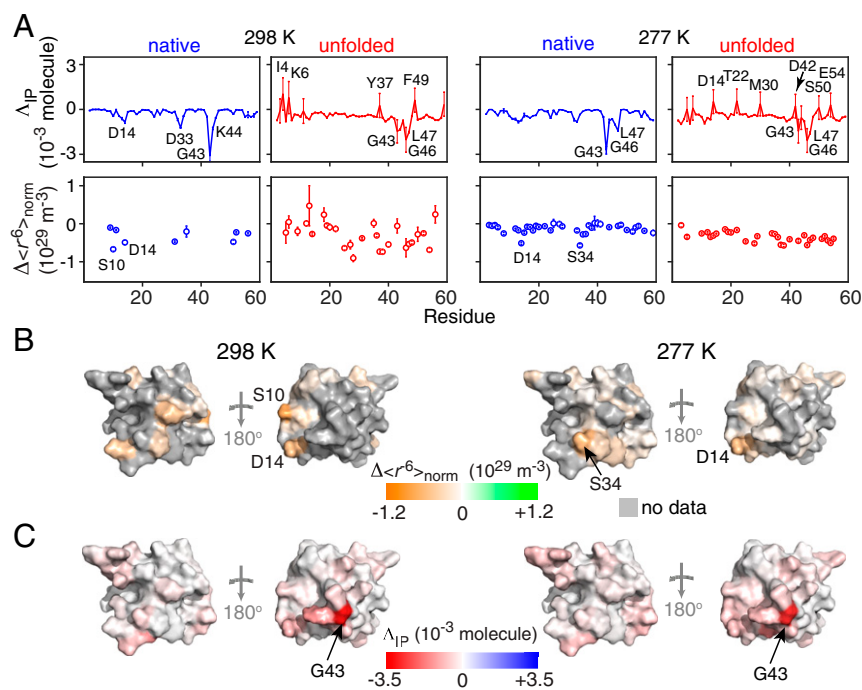
Fig. 7. Comparison of the local preferential interaction coefficient, Λ_{IP}, between Cl^- ions and backbone amide protons determined from MD simulations and the difference in $\langle r^{-6} \rangle_{norm}$ profiles between neutral and negatively charged paramagnetic cosolutes for the native and unfolded states of drkN SH3. (*A*) Λ_{IP} (*Top*) and $\Delta\langle r^{-6} \rangle_{norm}$ (*Bottom*) profiles at two temperatures (298 and 277 K). Λ_{IP} is defined by Eq. **11**; $\Delta\langle r^{-6} \rangle_{norm}$ is defined as [$\langle r^{-6} \rangle_{norm}$(3CX) − $\langle r^{-6} \rangle_{norm}$(3CY)], where 3CY and 3CX are 3-carbamoyl and 3-carboxy PROXYL, respectively. (*B*) $\Delta\langle r^{-6} \rangle_{norm}$ color graded on the molecular surface of native drkN SH3 from orange (−1.2 × 10²⁹ m⁻³ molecule) through white (0 × 10²⁹ m⁻³ molecule) to green (+1.2 × 10²⁹ m⁻³ molecule) (*C*) Λ_{IP} are color graded on the molecular surface of native drkN SH3 from red (−0.0035 molecule) through white (0 molecule) to blue (−0.0035 molecule). Residues that were not analyzed are shown in gray. The coordinates of native drkN SH3 are taken from PDB 2AZS (32), and the molecular surfaces were generated in the PyMol Molecular Graphics System (Version 2.0; Schröder LLC).

3-carbamoyl and 3-carboxyl PROXYL have very similar effects on the folding/unfolded equilibrium of drkN SH3, and there is little correlation between $\Delta\langle r^{-6} \rangle_{norm}$ (Fig. 7*B*) and the local preferential interaction coefficient Λ_{IP} (Fig. 7*C*) when both are visualized on a molecular surface of native drkN SH3.

In addition to $\langle r^{-6} \rangle_{norm}$, a residue-specific, correlation time τ_C is also obtained from analysis of the sPRE data (Fig. 4, *Bottom*, and Fig. 6, *Bottom*). τ_C has the simple qualitative interpretation that if τ_C is longer for one cosolute than another, then the residence time in the vicinity of the corresponding backbone amide group is longer for the former than the latter. At 298 K, τ_C is systematically longer for 3-carboxylate PROXYL than 3-carbamoyl PROXYL for the native state and systematically shorter for the unfolded state. At 277 K, however, the slope of the correlation between τ_C for 3-carboxylate and 3-carbamoyl PROXYL for both native and unfolded states is very close to 1, indicating that both cosolutes have the same residence times.

Effect of Temperature on Cosolute–Protein Interactions. A comparison of the effect of temperature on $\langle r^{-6} \rangle_{norm}$ is afforded by the correlation plots of $\langle r^{-6} \rangle_{norm}$ at 298 versus 277 K shown in Fig. 5 *C* and *D*. For the native state, the $\langle r^{-6} \rangle_{norm}$ correlation plots have a slope of about 1 for both paramagnetic cosolutes. Thus, for the native state, $\langle r^{-6} \rangle_{norm}$ is essentially independent of temperature, indicative of weak interactions or interactions with a small enthalpic contribution (49, 50) (*SI Appendix*). For the unfolded state, on the other hand, the slope of the correlation is greater than 1, and the $\langle r^{-6} \rangle_{norm}$ values tend to be higher at 298 than 277 K for both paramagnetic cosolutes. This result is suggestive of stronger interactions with an unfavorable enthalpic contribution between the cosolute and protein in the unfolded

state (49, 50) (*SI Appendix*). It is well known that hydrophobic association increases in strength with temperature with the enthalpic and entropic contributions being unfavorable and favorable, respectively, in this temperature range (51), so one might infer a hydrophobic character to the interactions. However, other interactions can also become stronger with temperature (52), and indeed, it has recently been argued this famous thermodynamic characteristic of the driving forces of protein folding may arise from hydrophilic interactions (53). It is unlikely that any potential small differences in the conformational space sampled by the ensemble of unfolded states at 298 and 277 contribute given that, from the replica exchange MD simulations, the radius of gyration decreases by less than 3% from 277 to 298 K (*SI Appendix*, Fig. S7*A*) and there is no observable difference in the calculated $\langle r^{-6} \rangle_{norm}^{exc}$ profiles at the two temperatures (*SI Appendix*, Fig. S7*B*)

Concluding Remarks. In the current work, we have probed the mechanism of cosolute denaturation at the atomic level by making use of our recently developed quantitative analysis of sPRE data (28) that yields information on paramagnetic cosolute protein interactions at atomic resolution to characterize preferential, ultra-weak interactions between a paramagnetic cosolute and the drkN SH3 protein domain that exists in dynamic equilibrium between native and unfolded states. Specifically, the sPRE data are analyzed in terms of an ansatz spectral density function (Eq. **8**) that satisfies the high- and low-frequency limits of the spectral density, to yield concentration normalized, equilibrium averages of the interspin distances, $\langle r^{-6} \rangle_{norm}$, between the unpaired electron on a paramagnetic cosolute and individual backbone amide protons of a protein, and the corresponding effective correlation times τ_C.

Okuno et al.
Atomic view of cosolute-induced protein denaturation probed by NMR solvent paramagnetic relaxation enhancement

PNAS | 7 of 9
https://doi.org/10.1073/pnas.2112021118
www.manaraa.com

Preferential cosolute–protein backbone interactions for native drkN SH3 predominantly involve solvent-exposed regions in loops. Outside of the loop regions, the cosolute–protein backbone interactions for the unfolded state are systematically stronger than those observed for the native state. Thus, the reduction of folding free energy by denaturant cosolutes likely involves stabilization of the unfolded state rather than destabilization of the native state. This is consistent with the finding from smFRET that the change of collapse free energy of the unfolded state mirrors the change in overall folding free energy with denaturant (6). Note that, on the other hand, some cosolutes, such as crowding agents or osmolytes, may increase the folding free energy by preferentially destabilizing the unfolded state (1). In addition, interactions involving the solvent-exposed indole ring of Trp36 are comparable to interactions with the backbone, indicating that side-chain contributions to the cosolvent effect should also be taken into account.

Although neutral (3-carbamoyl PROXYL) and negatively charged (3-carboxyl PROXYL) paramagnetic cosolutes show similar degrees of denaturation as monitored by smFRET, the interactions with the protein backbone amide groups are weaker for the latter than the former, as might be expected for a protein with an approximate overall charge −6. The apparently similar effect of both cosolutes on protein stability despite the difference in their overall interaction with the unfolded protein may arise from the challenge of quantitatively correcting the smFRET-derived stability for quenching by cosolutes, as well as from additional interactions with the unfolded protein not probed by backbone sPRE measurements. While we observed no significant temperature dependence for cosolute–native protein interactions, a sizeable temperature dependence was observed for the unfolded state with the strength of the interactions increasing with temperature, indicating enthalpically unfavorable association.

In this study, with the exception of the single tryptophan indole $N_{\varepsilon1}H$ group, we focused exclusively on cosolute–backbone amide interactions. A similar approach is also feasible for aliphatic groups of the protein, including side-chain methyl groups, in parallel with simulations including explicit cosolute molecules. We expect that further application of our approach to side-chain protons will provide further insight into elucidating the mechanism of the cosolvent effect.

Experimental Procedures

Details of protein expression and purification, sample conditions, smFRET and NMR experiments and their quantitative analysis, replica exchange MD simulations of the unfolded state of drkN SH3, and computation of $\langle r^{-6} \rangle_{norm}^{exc}$ for the native and unfolded states of drkN SH3 are provided in *SI Appendix*.

Units and Constants. n_S is in units of number of paramagnetic cosolvent molecules per cubic meter, given by the concentration in molar units multiplied by Avogadro's number times 10^3 (i.e., 6.022×10^{26}). The values of the various constants in Eqs. **3** and **4** are as follows: $\mu_o = 4\pi \times 10^{-7}$ T$^2 \cdot$m$^3 \cdot$J^{-1}; $\hbar = 1.05 \times 10^{-34}$ J$\cdot$s; $\gamma_H = 2.67 \times 10^8$ rad$\cdot$s$^{-1} \cdot$T^{-1}; and $\gamma_e = 1.76 \times 10^{11}$ rad$\cdot$s$^{-1} \cdot$T^{-1}.

Data Availability. All study data are included in the article and/or supporting information.

1. D. R. Canchi, A. E. García, Cosolvent effects on protein stability. *Annu. Rev. Phys. Chem.* **64**, 273–293 (2013).
2. C. Tanford, Isothermal unfolding of globular proteins in aqueous urea solutions. *J. Am. Chem. Soc.* **86**, 2050–2059 (1964).
3. C. Tanford, Protein denaturation. C. Theoretical models for the mechanism of denaturation. *Adv. Protein Chem.* **24**, 1–95 (1970).
4. J. A. Schellman, Fifty years of solvent denaturation. *Biophys. Chem.* **96**, 91–101 (2002).
5. D. W. Bolen, G. D. Rose, Structure and energetics of the hydrogen-bonded backbone in protein folding. *Annu. Rev. Biochem.* **77**, 339–362 (2008).
6. G. Ziv, G. Haran, Protein folding, protein collapse, and tanford's transfer model: Lessons from single-molecule FRET. *J. Am. Chem. Soc.* **131**, 2942–2947 (2009).
7. Y. Zhang, P. S. Cremer, Chemistry of Hofmeister anions and osmolytes. *Annu. Rev. Phys. Chem.* **61**, 63–83 (2010).
8. W. Zheng et al., Probing the action of chemical denaturant on an intrinsically disordered protein by simulation and experiment. *J. Am. Chem. Soc.* **138**, 11702–11713 (2016).
9. S. N. Timasheff, Thermodynamic binding and site occupancy in the light of the Schellman exchange concept. *Biophys. Chem.* **101-102**, 99–111 (2002).
10. J. A. Schellman, The thermodynamics of solvent exchange. *Biopolymers* **34**, 1015–1026 (1994).
11. S. Shimizu, J. J. Booth, S. Abbott, Hydrotropy: Binding models vs. statistical thermodynamics. *Phys. Chem. Chem. Phys.* **15**, 20625–20632 (2013).
12. X. Chen, L. B. Sagle, P. S. Cremer, Urea orientation at protein surfaces. *J. Am. Chem. Soc.* **129**, 15104–15105 (2007).
13. M. Auton, D. W. Bolen, Additive transfer free energies of the peptide backbone unit that are independent of the model compound and the choice of concentration scale. *Biochemistry* **43**, 1329–1342 (2004).
14. M. Auton, D. W. Bolen, Predicting the energetics of osmolyte-induced protein folding/unfolding. *Proc. Natl. Acad. Sci. U.S.A.* **102**, 15065–15068 (2005).
15. M. Auton, L. M. F. Holthauzen, D. W. Bolen, Anatomy of energetic changes accompanying urea-induced protein denaturation. *Proc. Natl. Acad. Sci. U.S.A.* **104**, 15317–15322 (2007).
16. X. Cheng et al., Experimental atom-by-atom dissection of amide–amide and amide–hydrocarbon interactions in H$_2$O. *J. Am. Chem. Soc.* **139**, 9885–9894 (2017).
17. X. Cheng, I. A. Shkel, K. O'Connor, M. T. Record, Jr., Experimentally determined strengths of favorable and unfavorable interactions of amide atoms involved in protein self-assembly in water. *Proc. Natl. Acad. Sci. U.S.A.* **117**, 27339–27345 (2020).
18. E. P. O'Brien, G. Ziv, G. Haran, B. R. Brooks, D. Thirumalai, Effects of denaturants and osmolytes on proteins are accurately predicted by the molecular transfer model. *Proc. Natl. Acad. Sci. U.S.A.* **105**, 13403–13408 (2008).
19. E. P. O'Brien, B. R. Brooks, D. Thirumalai, Molecular origin of constant *m*-values, denatured state collapse, and residue-dependent transition midpoints in globular proteins. *Biochemistry* **48**, 3743–3754 (2009).
20. W. Zheng, A. Borgia, M. B. Borgia, B. Schuler, R. B. Best, Empirical optimization of interactions between proteins and chemical denaturants in molecular simulations. *J. Chem. Theory Comput.* **11**, 5543–5553 (2015).
21. A. S. Holehouse, K. Garai, N. Lyle, A. Vitalis, R. V. Pappu, Quantitative assessments of the distinct contributions of polypeptide backbone amides versus side chain groups to chain expansion via chemical denaturation. *J. Am. Chem. Soc.* **137**, 2984–2995 (2015).
22. D. R. Canchi, D. Paschek, A. E. García, Equilibrium study of protein denaturation by urea. *J. Am. Chem. Soc.* **132**, 2338–2344 (2010).
23. D. R. Canchi, A. E. García, Backbone and side-chain contributions in protein denaturation by urea. *Biophys. J.* **100**, 1526–1533 (2011).
24. H. Hofmann et al., Polymer scaling laws of unfolded and intrinsically disordered proteins quantified with single-molecule spectroscopy. *Proc. Natl. Acad. Sci. U.S.A.* **109**, 16155–16160 (2012).
25. G. Hernández, C.-L. Teng, R. G. Bryant, D. M. LeMaster, O$_2$ penetration and proton burial depth in proteins: Applicability to fold family recognition. *J. Am. Chem. Soc.* **124**, 4463–4472 (2002).
26. G. Pintacuda, G. Otting, Identification of protein surfaces by NMR measurements with a pramagnetic Gd(III) chelate. *J. Am. Chem. Soc.* **124**, 372–373 (2002).
27. Z. Gong, C. D. Schwieters, C. Tang, Theory and practice of using solvent paramagnetic relaxation enhancement to characterize protein conformational dynamics. *Methods* **148**, 48–56 (2018).
28. Y. Okuno, A. Szabo, G. M. Clore, Quantitative interpretation of solvent paramagnetic relaxation for probing protein–cosolute interactions. *J. Am. Chem. Soc.* **142**, 8281–8290 (2020).
29. E. Spreitzer, S. Usluer, T. Madl, Probing surfaces in dynamic protein interactions. *J. Mol. Biol.* **432**, 2949–2972 (2020).
30. O. Zhang, L. E. Kay, J. P. Olivier, J. D. Forman-Kay, Backbone ^{1}H and ^{15}N resonance assignments of the N-terminal SH3 domain of drk in folded and unfolded states using enhanced-sensitivity pulsed field gradient NMR techniques. *J. Biomol. NMR* **4**, 845–858 (1994).
31. O. Zhang, J. D. Forman-Kay, Structural characterization of folded and unfolded states of an SH3 domain in equilibrium in aqueous buffer. *Biochemistry* **34**, 6784–6794 (1995).
32. I. Bezsonova, A. Singer, W.-Y. Choy, M. Tollinger, J. D. Forman-Kay, Structural comparison of the unstable drkN SH3 domain and a stable mutant. *Biochemistry* **44**, 15550–15560 (2005).
33. M. Tollinger, C. Neale, L. E. Kay, J. D. Forman-Kay, Characterization of the hydrodynamic properties of the folding transition state of an SH3 domain by magnetization transfer NMR spectroscopy. *Biochemistry* **45**, 6434–6445 (2006).
34. A. Mazouchi et al., Conformations of a metastable SH3 domain characterized by smFRET and an excluded-volume polymer model. *Biophys. J.* **110**, 1510–1522 (2016).
35. L. P. Hwang, J. H. Freed, Dynamic effects of pair correlation functions on spin relaxation by translational diffusion in liquids. *J. Chem. Phys.* **63**, 4017–4025 (1975).

36. Y. Ayant, E. Belorizky, P. Fries, J. Rosset, Effet des interactions dipolaires magnétiques intermoléculaires sur la relaxation nucléaire de molécules polyatomiques dans les liquides. *J. Phys. (Paris)* **38**, 325–337 (1977).

37. C. Sholl, Nuclear spin relaxation by translational diffusion in liquids and solids: High- and low-frequency limits. *J. Phys. C Solid State Phys.* **14**, 447 (1981).

38. P. H. Fries, Dipolar nuclear spin relaxation in liquids and plane fluids undergoing chemical reactions. *Mol. Phys.* **48**, 503–526 (1983).

39. B. Yu, C. C. Pletka, J. Iwahara, Quantifying and visualizing weak interactions between anions and proteins. *Proc. Natl. Acad. Sci. U.S.A.* **118**, e2015879118 (2021).

40. N. A. Farrow, O. Zhang, J. D. Forman-Kay, L. E. Kay, A heteronuclear correlation experiment for simultaneous determination of ^{15}N longitudinal decay and chemical exchange rates of systems in slow equilibrium. *J. Biomol. NMR* **4**, 727–734 (1994).

41. R. B. Best, W. Zheng, J. Mittal, Balanced protein-water interactions improve properties of disordered proteins and non-specific protein association. *J. Chem. Theory Comput.* **10**, 5113–5124 (2014).

42. Y.-K. Mok, C. M. Kay, L. E. Kay, J. Forman-Kay, NOE data demonstrating a compact unfolded state for an SH3 domain under non-denaturing conditions. *J. Mol. Biol.* **289**, 619–638 (1999).

43. K. A. Crowhurst, M. Tollinger, J. D. Forman-Kay, Cooperative interactions and a non-native buried Trp in the unfolded state of an SH3 domain. *J. Mol. Biol.* **322**, 163–178 (2002).

44. Y. Okuno *et al.*, Laser- and cryogenic probe-assisted NMR enables hypersensitive analysis of biomolecules at submicromolar concentration. *Proc. Natl. Acad. Sci. U.S.A.* **116**, 11602–11611 (2019).

45. E. J. Guinn, L. M. Pegram, M. W. Capp, M. N. Pollock, M. T. Record, Jr., Quantifying why urea is a protein denaturant, whereas glycine betaine is a protein stabilizer. *Proc. Natl. Acad. Sci. U.S.A.* **108**, 16932–16937 (2011).

46. Y. Luo, B. Roux, Simulation of osmotic pressure in concentrated aqueous salt solutions. *J. Phys. Chem. Lett.* **1**, 183–189 (2010).

47. L. Ma, L. Pegram, M. T. Record, Jr., Q. Cui, Preferential interactions between small solutes and the protein backbone: A computational analysis. *Biochemistry* **49**, 1954–1962 (2010).

48. A. E. Rydeen, E. M. Brustad, G. J. Pielak, Osmolytes and protein–protein interactions. *J. Am. Chem. Soc.* **140**, 7441–7444 (2018).

49. B. Yu, B. M. Pettitt, J. Iwahara, Dynamics of ionic interactions at protein–nucleic acid interfaces. *Acc. Chem. Res.* **53**, 1802–1810 (2020).

50. N. F. A. van der Vegt, D. Nayar, The hydrophobic effect and the role of cosolvents. *J. Phys. Chem. B* **121**, 9986–9998 (2017).

51. W. Kauzmann, Some factors in the interpretation of protein denaturation. *Adv. Protein Chem.* **14**, 1–63 (1959).

52. R. Wuttke *et al.*, Temperature-dependent solvation modulates the dimensions of disordered proteins. *Proc. Natl. Acad. Sci. U.S.A.* **111**, 5213–5218 (2014).

53. D. S. Tomar, M. E. Paulaitis, L. R. Pratt, D. N. Asthagiri, Hydrophilic interactions dominate the inverse temperature dependence of polypeptide hydration free energies attributed to hydrophobicity. *J. Phys. Chem. Lett.* **11**, 9965–9970 (2020).

BIOPHYSICS AND COMPUTATIONAL BIOLOGY

CHEMISTRY

Okuno et al.
Atomic view of cosolute-induced protein denaturation probed by NMR solvent paramagnetic relaxation enhancement

PNAS | **9 of 9**
https://doi.org/10.1073/pnas.2112021118

www.manaraa.com